





Magnetic field enhanced coercivity of Fe nanoparticles embedded in antiferromagnetic MnN films

Jinming Liu¹, Delin Zhang¹, Kai Wu¹, Xudong Hang²
and Jian-Ping Wang¹

¹ Department of Electrical and Computer Engineering, University of Minnesota, Minneapolis, MN 55455, United States of America

² Department of Chemical Engineering and Materials Science, University of Minnesota, Minneapolis, MN 55455, United States of America

E-mail: jpwang@umn.edu

Received 22 August 2019, revised 22 September 2019

Accepted for publication 9 October 2019


Published 1 November 2019



Abstract

The exchange coupling effect in nanocomposite samples with ferromagnetic (FM) body-centred tetragonal (bct) Fe nanoparticles (NPs) (~20 nm) embedded in an MnN antiferromagnetic (AFM) matrix is investigated. Both the bct Fe NPs control sample and the MnN (x nm)\bct Fe NPs\MnN (20–35 nm)\Ta (5 nm) nanocomposite samples are synthesized by a gas-phase condensation method. Both the coercivity and the remanence ratio of the nanocomposite samples are significantly enhanced compared with the bct Fe NPs sample. The coercivity and the remanence ratio increase with MnN thickness up to 30 nm and then decrease. Additionally, the exchange coupling strength between the bct Fe NPs and AFM MnN matrix is enhanced by magnetic field training. The magnetic field training leads to a higher coercivity and remanence ratio after one cycle of field-cooled hysteresis loop measurement. The coercivity of the composite sample increases by 80%, while the remanence ratio increases by around 30% compared with the bct Fe NPs sample. This work may provide an alternative approach to the design and manufacturing of FM-AFM exchange-coupled permanent magnets.

Keywords: magnetic nanoparticles, nanocomposite, bct Fe nanoparticles, antiferromagnetic MnN, permanent magnet

 Supplementary material for this article is available [online](#)

(Some figures may appear in colour only in the online journal)

1. Introduction

Embedding ferromagnetic nanoparticles (NPs) in a matrix could diversify their applications due to the interaction between the NPs and the matrix material [1–6]. In particular, the exchange coupling between antiferromagnets (AFM) and ferromagnets (FM) plays an essential role in many magnetoelectronic devices, such as the magnetic reader for hard disk drives [7], magnetoresistive random access memory [8], and magnetic biosensors [9]. In these applications, AFMs are used to magnetically pin the adjacent FM layer to induce a

unidirectional anisotropy. For AFM materials with high magnetic anisotropy, a hysteresis loop shift is produced [10]. While for AFM materials with low magnetic anisotropy, the AFM spins could be dragged by FM spins during magnetization reversal. In this process, extra energy is required to flip the magnetizations in both the positive and negative branches of the hysteresis loop. The hysteresis loop, as a result, shows an enhanced coercivity and remanence ratio [11]. Experimentally, the enhancement of exchange bias and coercivity could be observed simultaneously due to the distribution of grain size, defects, and anisotropies of the AFM and FM materials. More

details of exchange interactions between FM and AFM could be found in the review papers of this topic [12–14].

Although the interface exchange interaction between AFMs and FMs was first demonstrated from Co@CoO core-shell NPs in 1956 [15], there are limitations in the variety of this core-shell system, where the AFM shells are usually composed from native oxidation, with nitrides or sulfides for the FM core metal [16–18]. In the following decades, there have been few research works on the NPs exchange bias systems, while the main research focus has shifted towards thin films [19] as there are more choices of AFM materials for thin films than in the core-shell structures.

Recently, the study of the exchange effects on NP systems is attracting renewed interest, especially for the systems of FM NPs embedded in an AFM matrix due to significant improvements of fabrication techniques, such as the gas-phase condensation method [4, 20, 21]. These new techniques provide various AFM matrices for FM NPs which had hindered the research on FM/AFM core-shell systems previously. New application perspectives such as thermal stability enhancement of FM NPs, provide approaches to fabricate ultra-high areal density magnetic recording media [2], and to enhance the hard magnetic properties for magnets [1, 22].

In order to prepare nanocomposite samples with NPs embedded in a matrix, a system that could fabricate both NPs and matrix is required. The gas-phase condensation (GPC) system is an ideal candidate for preparing samples with NPs embedded in a matrix [4–6, 23, 24]. The GPC method is a well-controlled high vacuum technique in which NPs produced by a gas aggregation source are co-deposited with a matrix material using a dc sputtering source. The schematic drawing of the GPC system we used for preparing the samples in this paper is shown in figure 1 and can also be found in previous reports [25, 26]. The interfaces between FM NPs and the AFM matrix are free of contamination, which is critical for the FM/AFM exchange coupling investigation. Up to now, only a few groups have reported using this method to prepare FM/AFM nanocomposites (Ni NPs in an IrMn matrix, Co NPs in a Cr matrix, Fe NPs in a Cr matrix, etc) [6, 23, 27].

In this paper, body-centered tetragonal (bct) Fe NPs are the FM material and MnN is used for the AFM matrix for the nanocomposite samples. Fe is abundant on earth and its alloys are typically soft magnetic materials when they are in a body-centred-cubic (bcc) phase and they have been widely used in motors and transformers, whereas bct phase Fe shows high magnetocrystalline anisotropy [28, 29]. We have reported that the magnetic anisotropy of bct Fe NPs prepared by the GPC method was seven times higher than that of bcc Fe [30]. Antiferromagnetic MnN has a Néel temperature (T_N) of up to 600 K and is orders of magnitude cheaper than PtMn and IrMn. PtMn and IrMn have been commonly used for thin film exchange stacks [31]. Furthermore, MnN shows better corrosion resistance than FeMn and NiMn [32]. The high electrical resistivity of MnN makes it a good candidate for current in-plane magnetoresistance devices. The MnN (\times nm)\bct Fe NPs\MnN (\times nm)\Ta sandwich structure, named as Fe–MnN nanocomposite, was prepared by the GPC method with x ranging from 20 to 35 nm. Both the coercivity and the

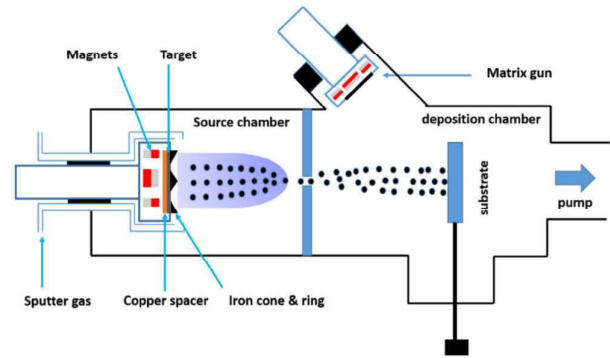


Figure 1. Schematic drawing of the GPC system synthesizing the nanocomposite sample with nanoparticles embedded in matrix.

remnance ratio of the Fe–MnN nanocomposite sample are enhanced when compared with the bct Fe NPs sample without the MnN matrix. Additionally, it is found that the exchange bias still exists at 10 K in the nanocomposite samples (see supplementary information (SI, available online at (stacks.iop.org/JPhysD/53/035003/mmedia)). We also report that a high magnetic field (up to 50 kOe) could enhance the exchange coupling between the FM bct Fe NPs and the AFM MnN matrix. It is observed that after measuring the first cycle of field-cooled hysteresis loops, the coercivities of the Fe–MnN nanocomposite samples increased. This increment depends on the thickness of the MnN matrix.

2. Methods

The details of the sample preparation and characterization are as follows. A dc sputtering based gas-phase condensation source was used to prepare the bct Fe NPs and a dc magnetron sputtering source was used to prepare the MnN thin films, as shown in figure 1. The working principle of the system can be found in [26, 30]. Argon gas was used as the sputtering gas for the bct Fe NPs. Argon and nitrogen gases were used for fabricating the MnN matrix films. A sandwich structure of the nanocomposite samples was made on an Si substrate\MnN (\times nm)\bct Fe NPs\MnN (\times nm)\Ta. The thicknesses of the two MnN layers were identical with x ranging from 20 to 35 nm. The deposition time of the bct Fe NPs for the nanocomposite samples was the same in order to produce consistent experimental results. A bct Fe NP sample with a stack of Si\bct Fe NPs\Ta was also prepared as the control sample. Here, Ta (\sim 5 nm) served as the capping layer to prevent oxidation.

A magnetic field of up to 6 kOe was applied parallel to the Si substrate during the sample fabrication process to induce a preferred magnetic orientation of the bct Fe NPs [11]. X-ray diffraction (XRD) patterns were taken with a Bruker 2D discover micro-diffractometer. The morphologies of the samples were measured by an FEI T12 (120 kV) transmission electron microscope (TEM). Magnetic characterization was done using a physical property measurement system (PPMS) integrated with a vibrating sample magnetometer (VSM) under varying temperatures from 10 K to 300 K.

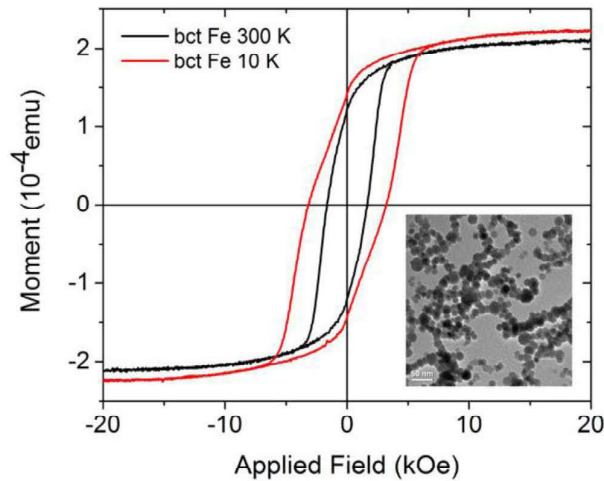


Figure 2. Hysteresis loops of bct Fe NPs measured at 300 K (black line) and 10 K (red line), respectively. The inset shows the TEM image of the bct Fe NPs.

3. Results and discussion

3.1. Magnetic properties and morphology of bct Fe NPs

The morphology and magnetic properties of the bct Fe NPs were investigated. The average size of the bct Fe NPs was around 20 nm as shown in the TEM image from the inset of figure 2. These NPs showed a spherical shape due to the high quenching rate during the formation of the bct Fe NPs. More details of the bct Fe NPs preparation and characterizations can be found in a previous report [30]. Hysteresis loops of the bct Fe NP sample were measured at 300 K and 10 K, respectively. The coercivity (H_c) was 1.6 kOe at 300 K and 3.2 kOe at 10 K, as shown in figure 2. Kinks were observed from the 10 K hysteresis loop since there were also some Fe NPs with body-centered cubic (bcc) structures in the bct Fe NP sample. The presence of bcc Fe NPs was due to the inhomogeneous magnetic field distribution along the etching track of the Fe target. The inhomogeneous field distribution could cause different quenching rates along the etching track of the Fe target. As a result, this led to bct Fe NPs at higher quenching rate regions and bcc Fe at lower quenching rate regions. These two phases were also confirmed by the XRD patterns, which can also be found in our previous report [30].

3.2. Crystal structure of MnN matrix

MnN thin films were prepared using the dc sputtering gun (matrix gun) as shown in figure 1. A silicon wafer was used as the substrate for the MnN films. The crystal structure of the MnN thin films was characterized by XRD, as shown in figure 3 in which MnN (002) and Si (400) peaks were observed. The pattern was consistent with the MnN XRD pattern reported previously [32], where MnN is the face-centered tetragonal structure and antiferromagnetic phase (AFM). The exchange bias and the enhancement of coercivity of the Fe–MnN nanocomposite samples was observed, further demonstrating the nature of MnN as an antiferromagnetic material.

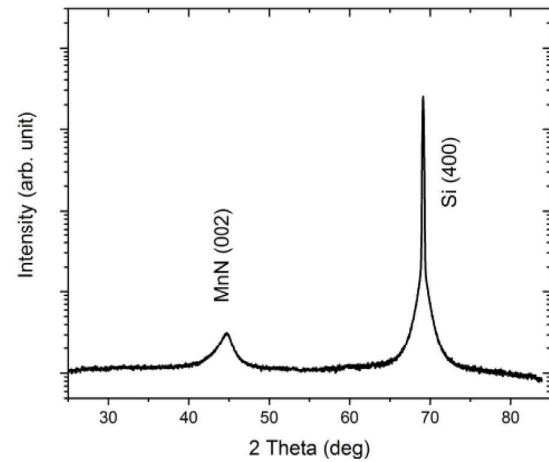


Figure 3. XRD pattern of the MnN thin film deposited by the dc sputtering gun.

3.3. Magnetic properties of Fe–MnN nanocomposites

3.3.1. Effects of MnN thickness. The magnetic properties of the Fe–MnN nanocomposite samples with different thicknesses of MnN layers were also characterized and compared with the bct Fe NPs. Hysteresis loops were measured for all nanocomposite samples at 300 K and 10 K, respectively. The results shown in figure 4 were from the hysteresis loops measured at the second cycle. Figure 4(a) showed the typical hysteresis loops of the Fe–MnN nanocomposite with 30 nm MnN. An enhanced H_c and remanence ratio (M_r/M_s) was obtained compared with the bct Fe NP sample (figure 2). The H_c has increased by 25% at 300 K and 82% at 10 K and the M_r/M_s ratio has increased by 21% at 300 K and 30% at 10 K. Figure 4(b) summarizes the MnN thickness dependence of the H_c and the M_r/M_s ratio of the nanocomposite samples. The results of the bct Fe NP sample are shown as the zero nm MnN in figure 4(b). The H_c and M_r/M_s ratio increased with MnN thickness up to 30 nm and then decreased significantly. This was in good agreement with the polycrystalline bilayer structure with MnN critical thickness around 30 nm [32].

The differences in H_c and M_r/M_s ratio from the Fe–MnN samples might be due to the change of the domain state magnetization of the AFM MnN layer. A model was proposed by Ali *et al* [33] to understand the thickness dependence of the coercivity and the exchange bias field in an AFM-FM exchange coupled system. There was a critical thickness for the domain wall stability of AFM materials. For an AFM layer below this critical thickness, the domain state magnetization of the AFM was reversible. In this case, additional coercivity with no exchange bias was obtained. When the AFM layer was at critical thickness, some of the domain state magnetizations became irreversible and exchange bias was observed along with reduced coercivity. Beyond this critical thickness, it became more difficult to form domain walls in the AFM layer, thus, larger domains may develop, which could decrease the bias field and coercivity. As discussed above, both exchange bias and coercivity enhancements could be observed experimentally due to the distribution of grain size,

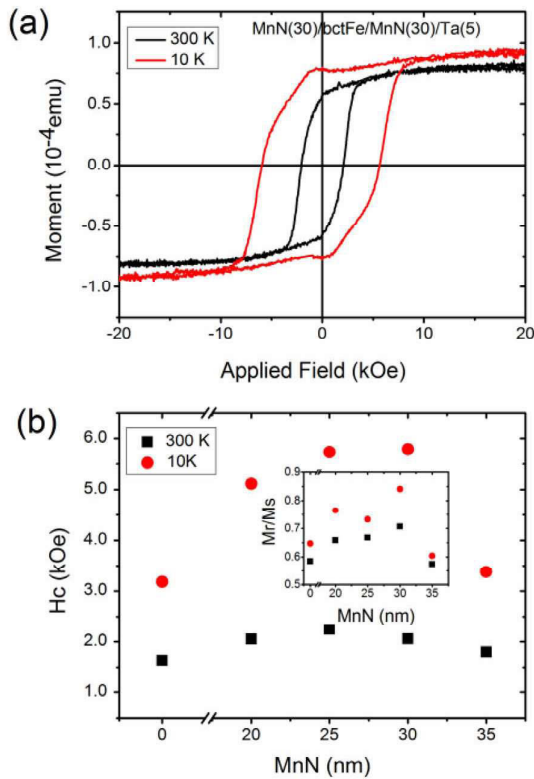


Figure 4. (a) Hysteresis loops of MnN nanocomposite when MnN is 30 nm thick. (b) H_c of MnN nanocomposites with different MnN thickness (0, 20, 25, 30, and 35 nm) and the inset is M_r/M_s versus MnN thickness. MnN (0 nm) stands for bct Fe NPs, shown in figure 2.

defects, and anisotropies of the AFM and FM materials. Some Fe–N surfaces might also form at the surface of the bct Fe NPs since N atoms were introduced during the growth of the MnN thin films. The Fe–N surface may also contribute to the magnetic properties of the Fe–MnN nanocomposites.

The Fe–MnN nanocomposite samples may follow this model. The enhancements of H_c and M_r/M_s ratio were due to the magnetically reversible or partially reversible MnN layers. The exchange bias was also observed from the Fe–MnN nanocomposite samples at 10 K. The exchange bias field was around 150 Oe for nanocomposite samples with 20, 25, and 30 nm MnN layers and decreased significantly for the nanocomposite sample with a 35 nm MnN layer, as shown in the SI figure S1. The M_s of Fe–MnN nanocomposite samples reduced slightly (2%–14%) compared with the M_s measured in the first cycle hysteresis loops. However, both the remanence and remanence ratio were improved in the second cycle hysteresis loops, as shown in SI figure S2. The critical thickness of MnN in the nanocomposite samples should be around 30–35 nm based on the model. The enhanced H_c and M_r/M_s ratio makes the Fe–MnN nanocomposites potential candidates for rare-earth-free magnets. The enhancement of H_c and M_r/M_s in AFM–FM samples is suitable for achieving higher magnetic energy products $(BH)_{\max}$. However, the M_s of the AFM–FM nanocomposite samples could be reduced compared to the FM phase alone since there is no contribution of M_s from the AFM

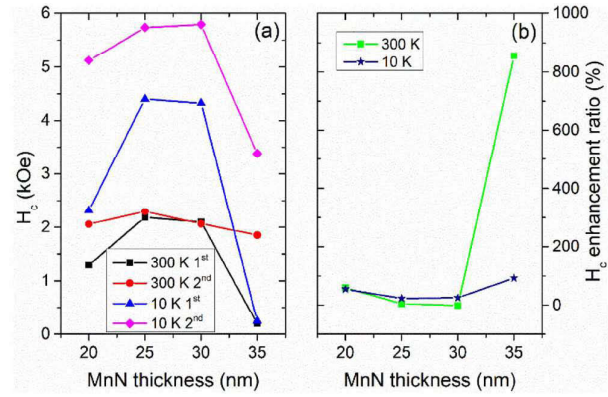


Figure 5. (a) The coercivity increase ratio of the first and second hysteresis loops versus MnN thickness measured at 300 K and 10 K, respectively. (b) The H_c enhancement at varying MnN thicknesses.

region. The decreased M_s in the AFM–FM nanocomposite samples is expected to lower the $(BH)_{\max}$. Modelling research is under way to quantify the trade-off between the enhanced H_c and M_r/M_s ratio and the reduced saturation magnetization after introducing AFM matrix in a magnet design [34].

3.3.2. Magnetic field training effect. The magnetic field training effect, which could help enhance the H_c and M_r/M_s ratio for the Fe–MnN nanocomposite samples, was investigated. The training effect usually refers to the gradual degradation of the exchange bias field and coercivity during subsequent hysteresis loop measurements. This effect is due to the deviation of the spin configuration of AFM from the equilibrium structure. The decrease of the exchange bias fields and coercivities with increasing hysteresis loop cycles is due to the rearrangement of the spin configuration to an equilibrium state [35]. For the Fe–MnN nanocomposite samples, the magnetic field (~6 kOe) applied during deposition assists the alignment of FM bct Fe NPs. However, it is not large enough to align the AFM MnN matrix. Thus, a higher magnetic field of up to 50 kOe was applied to the nanocomposite sample during the hysteresis loop measurement. The field enhances the exchange coupling between the FM bct Fe NPs and the AFM MnN matrix. Magnetic field cooling (50 kOe field) was performed on all the Fe–MnN nanocomposite samples from 300 K to 10 K. The hysteresis loops were measured with a magnetic field of up to 40 kOe along the same direction as the magnetic field applied during the growth of the nanocomposite samples. Several cycles of field-cooled (50 kOe) hysteresis loops were measured at both 300 K and 10 K to study the magnetic training effect which is usually observed in AFM–FM systems. The coercivities and remanence ratios of the Fe–MnN nanocomposite samples increased in the second cycle of hysteresis loops, as shown in figure 5(a). The magnetic field around ~6 kOe during sample growth could induce the easy axis alignment for the bct Fe NPs. For the as-deposited Fe–MnN nanocomposite sample, it might not be at its lowest free energy state. After the 50 kOe magnetic field training, these samples are at their lowest energy state with stable magnetic performances. Thus, the coercivities and remanence ratios of

the Fe–MnN nanocomposite samples remained constant for the subsequent cycles, indicating the AFM spin configuration was already in the equilibrium state. The enhancement of H_c was due to a better magnetic alignment between the FM bct Fe NPs and the AFM MnN matrix after measurements of the first hysteresis loops at 300 K and 10 K.

A high magnetic field, in principle, could help rearrange the spin configurations of the MnN thin film matrix. The effective anisotropy constant of MnN was reported to be around $2.4 \times 10^5 \text{ erg cm}^{-3}$ (24 kJ m^{-3}) in a thin film sample [36], which is relatively small compared with other AFM materials such as IrMn. The applied magnetic field $\sim 50 \text{ kOe}$ helped to at least partially enhance the exchange coupling between the AFM MnN matrix and the FM bct Fe NPs [37, 38]. Thus, the enhancement of coercivity and remanence ratio was obtained for the hysteresis loops measured at the second cycle. For the hysteresis loops measured in the subsequent cycles, the alignment between ferromagnetic nanoparticles and the antiferromagnetic matrix was already built, and there was no further increase of H_c .

The H_c enhancement ratio after field training also depended on the MnN thickness. Figure 5(a) shows the H_c enhancement of the nanocomposite samples after the second cycle measurement of hysteresis loops with different MnN thickness at 300 K and 10 K, respectively. The enhancement was observed in all the nanocomposite samples, as shown in figure 5(b) with a minimum of around 30 nm MnN. Therefore, the critical AFM MnN thickness for Fe–MnN nanocomposite samples should be around 30–35 nm since the coercivity started decreasing dramatically in that range. When the MnN thickness was 35 nm, the coercivity enhancement ratio increased significantly compared to other nanocomposite samples with thinner MnN layers. However, the coercivity of the sample decreased significantly. For 35 nm MnN, some irreversible and large domains may develop in the AFM MnN layers. In this case, the coercivity was low in the first cycle, as revealed in figure 5(a). After the first cycle of hysteresis loops, some MnN grains were exchange coupled to the bct Fe NPs, leading to an enhanced coercivity in the second cycle. Although the coercivity of the Fe–MnN nanocomposite sample with 35 nm MnN was small, the coercivity enhancement ratio was high due to the rearrangements of the AFM MnN spin structures.

4. Conclusions

In summary, Fe–MnN nanocomposite samples were synthesized using a gas-phase condensation method. The prepared samples demonstrated higher coercivity (with an increase of up to 82%) and remanence ratio (up to 30% higher) than that of bct Fe NPs due to exchange coupling between the FM bct Fe NPs and the AFM MnN matrix. Nanocomposite samples with different MnN thicknesses from 20 nm to 35 nm were investigated. The enhancements of coercivity and remanence ratio were dependent on the MnN thickness, which was due to the reversible part of the AFM MnN matrix. Magnetic field training could enhance the exchange coupling effect between the AFM MnN matrix and the FM bct Fe NPs. Thus, enhanced

coercivity and remanence ratio were obtained after one cycle of hysteresis loop measurements. Such an enhancement could enable Fe–MnN nanocomposites to be a potential candidate for rare-earth-free magnets.

Acknowledgments

Parts of this work were carried out in the Characterization Facility, University of Minnesota, a member of the NSF-funded Materials Research Facilities Network (www.mrnf.org) via the MRSEC program. The authors thank the partial support from the Institute for Rock Magnetism, Department of Earth Science, University of Minnesota, Twin Cities, for the use of instruments. Jian-Ping Wang gives thanks for the support of the Robert Hartmann endowed chair professorship.

ORCID iDs

Jinming Liu  <https://orcid.org/0000-0002-4313-5816>

Kai Wu  <https://orcid.org/0000-0002-9444-6112>

Xudong Hang  <https://orcid.org/0000-0001-6296-7178>

Jian-Ping Wang  <https://orcid.org/0000-0003-2815-6624>

References

- [1] Sort J, Nogués J, Suriñach S, Muñoz J S, Baró M D, Chappell E, Dupont F and Chouteau G 2001 Coercivity and squareness enhancement in ball-milled hard magnetic-antiferromagnetic composites *Appl. Phys. Lett.* **79** 1142–4
- [2] De Toro J A, Marques D P, Muñoz P, Skumryev V, Sort J, Givord D and Nogués J 2015 High temperature magnetic stabilization of cobalt nanoparticles by an antiferromagnetic proximity effect *Phys. Rev. Lett.* **115** 057201
- [3] Tobia D, Winkler E, Zysler R D, Granada M, Troiani H E and Fiorani D 2009 Exchange bias of Co nanoparticles embedded in Cr_2O_3 and Al_2O_3 matrices *J. Appl. Phys.* **106** 103920
- [4] Liu X, He S, Qiu J and Wang J 2011 Nanocomposite exchange-spring magnet synthesized by gas phase method: from isotropic to anisotropic *Appl. Phys. Lett.* **98** 222507
- [5] Laureti S, Peddis D, Del Bianco L, Testa A M, Varvaro G, Agostinelli E, Binns C, Baker S, Qureshi M and Fiorani D 2012 Exchange bias and magnetothermal properties in Fe@Mn nanocomposites *J. Magn. Magn. Mater.* **324** 3503–7
- [6] Kuerbanjiang B, Wiedwald U, Haering F, Biskupek J, Kaiser U, Ziemann P and Herr U 2013 Exchange bias of Ni nanoparticles embedded in an antiferromagnetic IrMn matrix *Nanotechnology* **24** 455702
- [7] Chappert C, Fert A and Van Dau F N 2007 The emergence of spin electronics in data storage *Nat. Mater.* **6** 813–23
- [8] Gaidis M C 2010 Magnetoresistive random access memory *Proc. IEEE* **104** 1796–830
- [9] Feng Y, Liu J, Klein T, Wu K and Wang J-P 2017 Localized detection of reversal nucleation generated by high moment magnetic nanoparticles using a large-area magnetic sensor *J. Appl. Phys.* **122** 123901
- [10] Berkowitz A E, Sinha S K, Fullerton E E and Smith D J 2015 Exchange bias mediated by interfacial nanoparticles (invited) *J. Appl. Phys.* **117** 172607
- [11] Nogués J, Sort J, Langlais V, Skumryev V, Suriñach S, Muñoz J S and Baró M D 2005 Exchange bias in nanostructures *Phys. Rep.* **422** 65–117

- [12] Nogués J and Schuller I K 1999 Exchange bias *J. Magn. Magn. Mater.* **192** 203–32
- [13] Berkowitz A E and Takano K 1999 Exchange anisotropy—a review *J. Magn. Magn. Mater.* **200** 552–70
- [14] O’Grady K, Fernandez-Outon L E and Vallejo-Fernandez G 2010 A new paradigm for exchange bias in polycrystalline thin films *J. Magn. Magn. Mater.* **322** 883–99
- [15] Meiklejohn W H and Bean C P 1957 New magnetic anisotropy *Phys. Rev.* **105** 904–13
- [16] Prados C, Multigner M, Hernando A, Sánchez J C, Fernández A, Conde C F and Conde A 1999 Dependence of exchange anisotropy and coercivity on the Fe–oxide structure in oxygen-passivated Fe nanoparticles *J. Appl. Phys.* **85** 6118–20
- [17] Lin H-M, Hsu C M, Yao Y D, Cben Y Y, Kuan T T, Yang F A and Tung C Y 1995 Magnetic study of both nitrided and oxidized CO particles *Nanostruct. Mater.* **6** 977–80
- [18] Bienenstock A 1961 Determination of crystallite size distributions from x-ray line broadening *J. Appl. Phys.* **32** 187–9
- [19] Stamps R L 2000 Mechanisms for exchange bias *J. Phys. D: Appl. Phys.* **33** R247–68
- [20] Skumryev V, Stoyanov S, Zhang Y, Hadjipanayis G, Givord D and Nogués J 2003 Beating the superparamagnetic limit with exchange bias *Nature* **423** 850–3
- [21] Sort J, Langlais V, Doppiu S, Dieny B, Suriñach S, Muñoz J S, Baró M D, Laurent C and Nogués J 2004 Exchange bias effects in Fe nanoparticles embedded in an antiferromagnetic Cr₂O₃ matrix *Nanotechnology* **15** S211–4
- [22] Sort J, Suriñach S, Muñoz J S, Baró M D, Nogués J, Chouteau G, Skumryev V and Hadjipanayis G C 2002 Improving the energy product of hard magnetic materials *Phys. Rev. B* **65** 174420
- [23] Qureshi M T, Baker S H, Binns C, Roy M, Laureti S, Fiorani D and Peddis D 2015 Structure and magnetic properties of Fe nanoparticles embedded in a Cr matrix *J. Magn. Magn. Mater.* **378** 345–52
- [24] Peddis D, Qureshi M T, Baker S H, Binns C, Roy M, Laureti S, Fiorani D, Nordblad P and Mathieu R 2015 Magnetic anisotropy and magnetization dynamics of Fe nanoparticles embedded in Cr and Ag matrices *Phil. Mag.* **95** 3798–807
- [25] Jing Y, He S H and Wang J P 2013 Composition-and phase-controlled high-magnetic-moment Fe_{1-x}Co_x nanoparticles for biomedical applications *IEEE Trans. Magn.* **49** 197–200
- [26] Liu J, Wu K and Wang J-P 2016 Magnetic properties of cubic FeCo nanoparticles with anisotropic long chain structure *AIP Adv.* **6** 056126
- [27] Baker S H, Kurt M S, Roy M, Lees M R and Binns C 2016 Structure and magnetism in Cr-embedded Co nanoparticles *J. Phys.: Condens. Matter* **28** 046003
- [28] Burkert T, Eriksson O, James P, Simak S I, Johansson B and Nordström L 2004 Calculation of uniaxial magnetic anisotropy energy of tetragonal and trigonal Fe, Co, and Ni *Phys. Rev. B* **69** 104426
- [29] Burkert T, Nordström L, Eriksson O and Heinonen O 2004 Giant magnetic anisotropy in tetragonal FeCo alloys *Phys. Rev. Lett.* **93** 027203
- [30] Liu J, Schliep K, He S H, Ma B, Jing Y, Flannigan D J and Wang J P 2018 Iron nanoparticles with tunable tetragonal structure and magnetic properties *Phys. Rev. Mater.* **2** 054415
- [31] Leineweber A, Niewa R, Jacobs H and Kockelmann W 2000 The manganese nitrides η -Mn₃N₂ and θ -Mn₆N_{5+x}: nuclear and magnetic structures *J. Mater. Chem.* **10** 2827–34
- [32] Meinert M, Bükler B, Graulich D and Dunz M 2015 Large exchange bias in polycrystalline MnN/CoFe bilayers at room temperature *Phys. Rev. B* **92** 144408
- [33] Ali M, Marrows C H, Al-Jawad M, Hickey B J, Misra A, Nowak U and Usadel K D 2003 Antiferromagnetic layer thickness dependence of the IrMn/Co exchange-bias system *Phys. Rev. B* **68** 214420
- [34] Hang X and Wang J-P 2019 Permanent magnet design assisted by antiferromagnet-ferromagnet coupling: a Monte Carlo study *J. Appl. Phys.* submitted
- [35] Binek C, He X and Polisetty S 2005 Temperature dependence of the training effect in a Co/CoO exchange-bias layer *Phys. Rev. B* **72** 054408
- [36] Zilske P, Graulich D, Dunz M and Meinert M 2017 Giant perpendicular exchange bias with antiferromagnetic MnN *Appl. Phys. Lett.* **110** 192402
- [37] Vallejo-Fernandez G, Fernandez-Outon L E and O’Grady K 2007 Measurement of the anisotropy constant of antiferromagnets in metallic polycrystalline exchange biased systems *Appl. Phys. Lett.* **91** 212503
- [38] Aley N P, Vallejo-Fernandez G, Kroege R, Lafferty B, Agnew J, Lu Y and O’Grady K 2008 Texture effects in IrMn/CoFe exchange bias systems *IEEE Trans. Magn.* **44** 2820–3